Nucleation, Growth, and Aggregation of Alumina Inclusions in Steel

WEN YANG,[1] HAOJIAN DUAN,[1] LIFENG ZHANG,[1,2] and YING REN[1]

1.—School of Metallurgical and Ecological Engineering, University of Science and Technology Beijing, Beijing 100083, People's Republic of China. 2.—e-mail: zhanglifeng@ustb.edu.cn

Whether a nonmetallic inclusion is detrimental to steel properties or not depends on its size. The final size of an inclusion in steel is influenced by several factors, including nucleation, growth, and aggregation. In the current work, the thermodynamics for homogeneous nucleation of alumina was calculated, and the three-dimensional alumina morphologies after Al deoxidation were observed in laboratory. It is indicated by the calculation that, when the interfacial tension between steel melt and alumina is higher or the nucleus radius is larger, it is harder for alumina to nucleation. One minute after the deoxidation, many single-alumina particles with different shapes, including spherical, dendritic, flower, plate-like, and irregular, were observed. The formation of various shapes is due to different growth mechanisms. During the holding process after deoxidation, several types of aggregation morphologies were observed, such as disorderly type and regular type. Owing to the effects of sintering and Ostwald ripening, the aggregated inclusions changed from angular shape to smooth coral shape.

INTRODUCTION

Nonmetallic inclusions, which are inevitable in steel, have either a detrimental or a beneficial effect on the quality of steels. For example, on the one hand, large inclusions, especially alumina-based inclusions, will deposit on the submerged entry nozzle (SEN) of mold, which causes the unstable casting and induces the crack defects on slab and the sliver and scab defects on steel sheets.[1–4] On the other hand, some nonmetallic inclusions, especially fine second-phase particles, act as grain-growth inhibitors during the primary and secondary recrystallization, and make fine grains of steel.[5] Furthermore, in recent years, some small oxides were used to induce the formation of intra-granular ferrite (IGF), which is called "oxide metallurgy," to refine the grain and improve the strength of steel.[6–8]

Whether an inclusion is detrimental or not depends on its size. The formation of inclusions is based on the thermodynamics, and those of some types of inclusions have been studied in which the classic equilibrium state was considered.[9–11] The final size of an inclusion in steel is influenced by several factors, including the nucleation, the growth by element diffusion, and the aggregation by collision. The behaviors mentioned based on dynamics have been studied by many researchers mainly using the method of numerical simulation and calculation.[12–14] For example, the inclusion characteristic in forms of size, quantity, and distribution in the ladle during secondary refining and in the tundish[15] and mold[16] during continuous casting were well studied in recent years using commercial software, such as CFX (ANSYS Inc., Canonsburg, PA), ANSYS (ANSYS Inc., Canonsburg, PA), and Fluent (ANSYS Inc., Canonsburg, PA). However, there is a lack of more practical and clear evidence to present the details of the process.[17,18]

In this article, the alumina inclusion is taken as a case. The thermodynamics for homogeneous nucleation of alumina is calculated considering the interfacial tension between the inclusion and steel melts. Then several types of alumina morphologies as a function of holding time after deoxidation reaction by aluminum are presented based on the laboratory experiments.

THERMODYNAMICS OF ALUMINA NUCLEATION

In the classic thermodynamic theory of oxide formation, it is assumed that the oxide inclusions

can be formed at equilibrium state when the generated free energy change equals zero. However, actually, a small amount of additional energy is needed for the inclusion formation due to the increased interfacial energy between the new phase and the steel melt. Thus, the nucleation work is considered to build the thermodynamics of homogeneous nucleation of alumina.

Effect of Interfacial Tension on the Nucleation of Al_2O_3

The formation reaction of Al_2O_3 is described as[10]:

$$(Al_2O_3) = 2[Al] + 3[O] \tag{1}$$
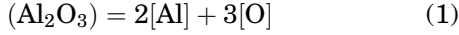
$$\log K = 11.62 - 45300/T \tag{2}$$

$$K = \frac{a_{Al}^2 \cdot a_O^3}{a_{Al_2O_3}} \tag{3}$$

$$\log K = 2\log f_{Al} + 2\log[\%Al] + 3\log f_O + 3\log[\%O] + \log a_{Al_2O_3} \tag{4}$$

where K is the equilibrium constant based on 1% mass fraction of Henry's standard state. a_{Al} and a_O are the activities of Al and O in the melt based on 1% mass fraction of Henry's standard state. $a_{Al_2O_3}$ is the activity of Al_2O_3 whose standard state is taken as pure solid, and the value is assumed to be unity.$[\%i]$ is the mass percentage of element i. f_i is the activity coefficient of element i based on 1% mass fraction of Henry's standard state. f_i can be calculated by the following equations where both the first-order and the second-order activity interaction coefficients listed in Table I are considered.

$$\log f_{Al} = e_{Al}^{Al}[\%Al] + e_{Al}^{O}[\%O] + r_{Al}^{O}[\%O]^2 + r_{Al}^{Al_2O_3}[\%Al][\%O] \tag{5}$$

$$\log f_{O} = e_{O}^{Al}[\%Al] + e_{O}^{O}[\%O] + r_{O}^{Al}[\%Al]^2 + r_{O}^{Al_2O_3}[\%Al][\%O] \tag{6}$$

Thus, the following equation can be derived from Eqs. 4–6:

$$\log K = (2e_{Al}^{Al} + 3e_{O}^{Al})[\%Al] + (2e_{Al}^{O} + 3e_{O}^{O})[\%O] + 2\log[\%Al] + 3\log[\%O] + 2r_{Al}^{O}[\%O]^2 + 3r_{O}^{Al}[\%Al]^2 + (2r_{Al}^{Al_2O_3} + 3r_{O}^{Al_2O_3})[\%Al][\%O] \tag{7}$$

The $[\%O]$ in Eq. 7 is the equilibrium oxygen content for Al_2O_3 formation without considering the nucleation.

As the nucleation of Al_2O_3 is considered, the Gibbs free energy change of the system includes not only the

free energy change of the deoxidation reaction but also the free energy change during the nucleation of Al_2O_3. The nucleation would not occur until the required supersaturation of the elements is achieved. According to Elliott,[19] with respect to the equilibrium without considering the nucleation ($\sigma = 0$), when the effect of interfacial tension on the nucleation is considered, the critical supersaturation, that is, the required Gibbs free energy change for nucleation, can be represented by the following equation:

$$\Delta G_{hom}^{crit} = G - G_{eq} = -RT \ln[(f_O[\%O])^3 (f_{Al}[\%Al])^2] - \{-RT \ln[(f_O[\%O])_{eq}^3 (f_{Al}[\%Al])_{eq}^2]\} \tag{8}$$

The following equation can be arranged by substituting Eqs. 5 and 6:

$$\Delta G_{hom}^{crit} = -2.303RT\{ (2e_{Al}^{Al} + 3e_{O}^{Al})([\%Al] - [\%Al]_{eq}) + (2e_{Al}^{O} + 3e_{O}^{O})([\%O] - [\%O]_{eq}) + 2(\log[\%Al] - \log[\%Al]_{eq}) + 3(\log[\%O] - \log[\%O]_{eq}) + 2r_{Al}^{O}([\%O]^2 - [\%O]_{eq}^2) + 3r_{O}^{Al}([\%Al]^2 - [\%Al]_{eq}^2) + (2r_{Al}^{Al_2O_3} + 3r_{O}^{Al_2O_3})([\%Al][\%O] - [\%Al]_{eq}[\%O]_{eq})\} \tag{9}$$

At a constant concentration of aluminum, the equation above can be simplified as follows:

$$\Delta G_{hom}^{crit} = -2.303RT\{ (2e_{Al}^{O} + 3e_{O}^{O})([\%O] - [\%O]_{eq}) + 3(\log[\%O] - \log[\%O]_{eq}) + 2r_{Al}^{O}([\%O]^2 - [\%O]_{eq}^2) + (2r_{Al}^{Al_2O_3} + 3r_{O}^{Al_2O_3})[\%Al]([\%O] - [\%O]_{eq})\} \tag{10}$$

According to Elliott,[19] the critical supersaturation in terms of the free energy for homogeneous nucleation is:

$$\Delta G_{hom}^{crit} = -2.7V(\sigma^3/kT\log A)^{1/2} \tag{11}$$

where ΔG_{hom}^{crit} is the critical supersaturation for homogeneous nucleation; V is the molar volume of the new phase and for Al_2O_3 the value is approximately

Table I. First- and second-order activity interaction coefficients used in this work[10]

First order	Second order
$e_O^O = 0.76 - 1750/T$	$r_{Al}^O = -107 + 275,000/T$
$e_{Al}^{Al} = 80.5/T$	$r_O^{Al} = 0.0033 - 25.0/T$
$e_{Al}^O = 3.21 - 9720/T$	$r_{Al}^{Al_2O_3} = -0.021 - 13.78/T$
$e_O^{Al} = 1.90 - 5750/T$	$r_O^{Al_2O_3} = 127.3 + 327,300/T$

25.6×10^{-6} m³/mol; σ is the interfacial tension between the matrix and the new phase; k is Boltzmann's constant; T is the temperature (K); and A is the frequency factor, the value of which for Al_2O_3 is 10.[26]

Combining Eqs. 2, 7, 10, and 11, the critical values of aluminum and oxygen in steel melt for the nucleation of Al_2O_3 at different interfacial tensions can be calculated, as shown in Fig. 1, where some experimental data measured by other researchers[20–24] are presented as well. It is indicated that under a certain content of aluminum, higher oxygen content is required for Al_2O_3 nucleation at higher interfacial tension, which means it is more difficult to achieve nucleation at higher interfacial tension. Comparing the calculated curves with the measured data, it is somehow confirmed that a supersaturation is needed for the nucleation, and it is estimated that the interfacial tension between liquid iron and Al_2O_3 in the experiments is approximately 0.5–1.5 N/m. The scattered experimental data may be due to the difference of experimental conditions between the studies. There were also many experimental results, which are not shown in the figure, which were located near the curve of $\sigma = 0$. Those may be at the situation of heterogeneous nucleation.

Effect of Nucleus Radius on the Nucleation of Al_2O_3

According to Wasai and Mukai,[25,26] the relationship between the interfacial tension between iron and Al_2O_3 and the nucleus radius of Al_2O_3 can be expressed as:

$$\sigma_0/\sigma = (1/V)/((2\Gamma/r) + (1/V)) \tag{12}$$

where σ_0 is the interfacial tension of an alumina particle with radius r; σ is the interfacial tension when r is infinity (in iron melts, σ is 2.328 N/m); V is the molar volume of alumina (m³/mol); and Γ is the surface excess (mol/m²), $\Gamma = N^{-1/3}V^{-2/3}$ (N is Avogadro's number).

The change of interfacial tension between iron and alumina as a function of radius of the alumina particle is shown in Fig. 2, indicating that the interfacial tension decreases with decreasing the radius, especially when the radius is smaller than 10^{-8} m.
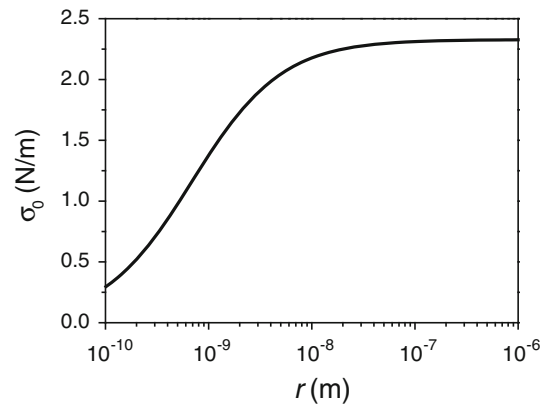

Fig. 2. The change of interfacial tension between iron and alumina as a function of the radius of the alumina particle.
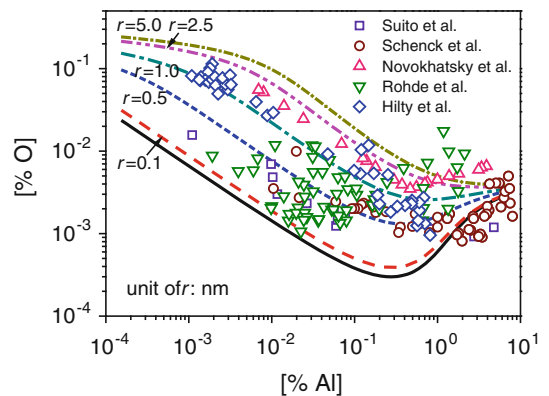
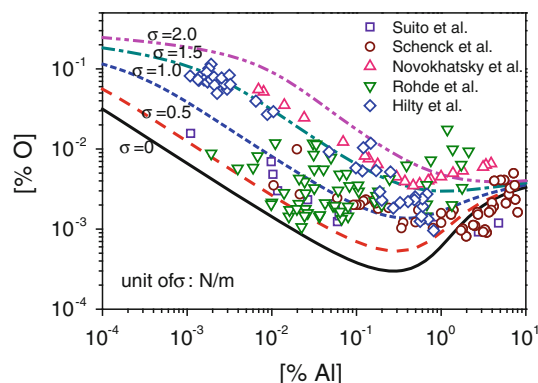

Fig. 3. Effect of nucleus radius on the nucleation of Al_2O_3.

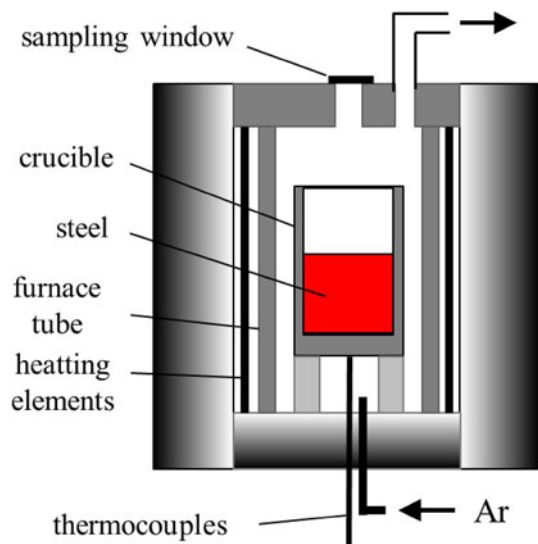Fig. 1. Effect of interfacial tension on the nucleation of Al_2O_3.

Fig. 4. Schematic of experimental apparatus.

Similar to the derivation process in the previous section, the Al-O equilibrium curve at a different nucleus radius can be calculated and shown in Fig. 3. Many experimental data reported[20–24] are

Table II. Composition of steel before melting (wt.%)

C	Si	Mn	P	S
0.05	0.01	0.18	0.006	0.005

included in the figure as well. It is indicated that when the nucleation radius is larger, a higher content of oxygen and aluminum is required for the nucleation of Al_2O_3; in other words, it is more difficult to achieve nucleation at a larger nucleation radius. On the other hand, the possible nucleus radius could be estimated according to the concentration of aluminum and oxygen. Comparing the measured data with the calculated curves, it is estimated that the nucleus radius during the nucleation of Al_2O_3 is approximately 0.5–1.5 nm. Since the nucleus radius is too small and the
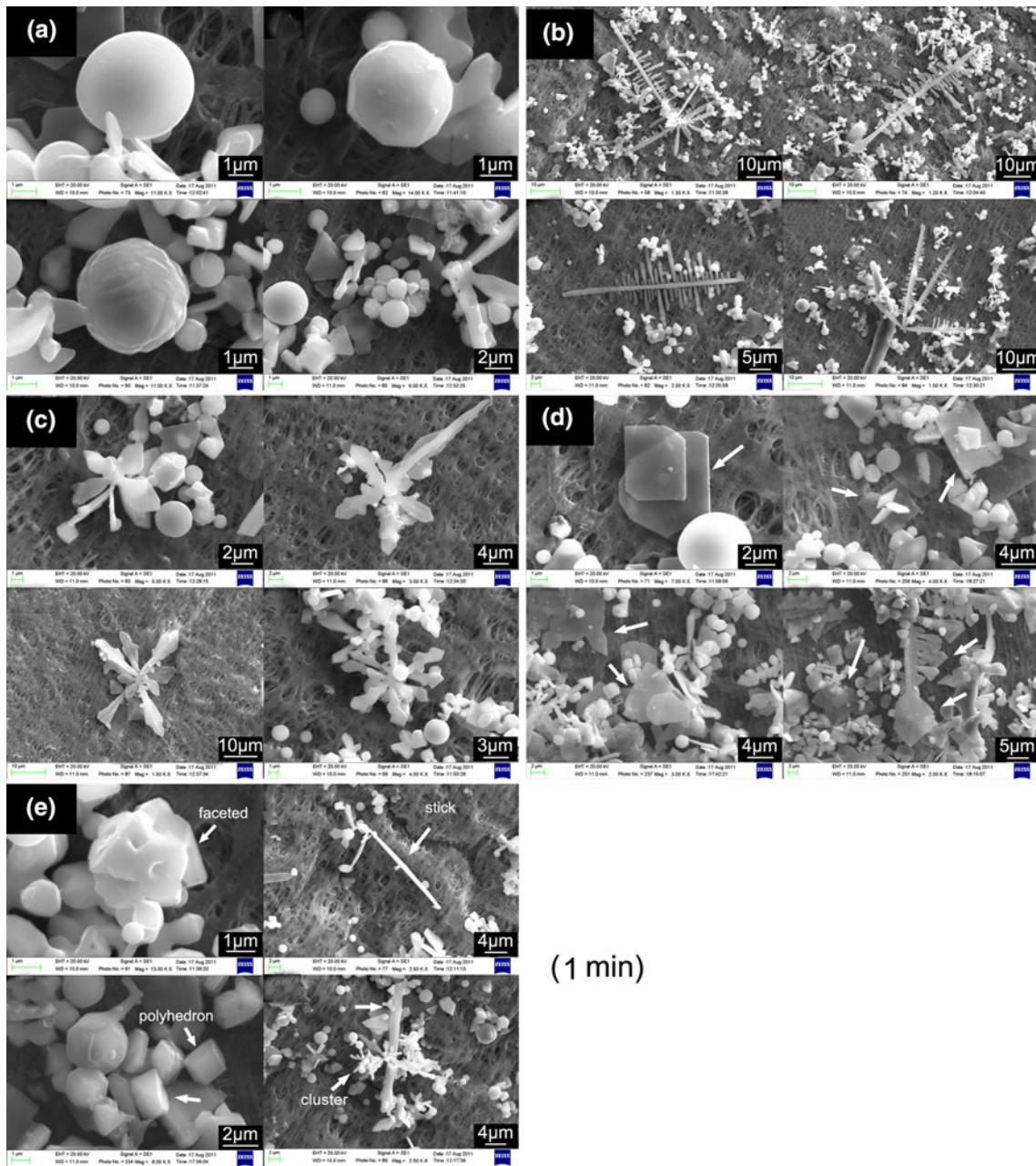

Fig. 5. Three-dimensional morphologies of extracted inclusions observed in the sample with a holding time of 1 min: (a) spherical, (b) dendritic, (c) flower, (d) plate-like (marked by white arrows), and (e) irregular (faceted, stick-like, polyhedral, and cluster). White and gray inclusions located on the dark gray filter.

nucleation rate is extremely great, it is hard to measure the nucleation process directly.

THREE-DIMENSIONAL OBSERVATION OF GROWTH AND AGGREGATION OF ALUMINA

After nucleation, the nuclei will grow by Ostwald ripening and Brownian diffusion. Meanwhile, the size increases from nano-scale to micron scale. During the growth, many different shapes of particles will exist resulting from the difference of growing conditions. When the size of particles increases to micron scale, the growth of some inclusions will change to aggregation. In the current work, the growth and aggregation phenomena of alumina were observed by laboratory experiment.

Experimental

Deoxidation experiments were carried out in a silicon-molybdenum resistance furnace, as shown in Fig. 4. Approximately 500 g of low-carbon steel with its composition shown in Table II was melted in a MgO crucible under a purified argon atmosphere at 101 kPa and 1873 K. Fe_2O_3 powders were added to the melt to adjust oxygen activity to approximately 0.03% in Henry law's standard.

After 10 min of stabilization of the melt, the oxygen activity was measured using a zirconia-type sensor. Then Al wires ($\phi = 0.7$ mm) were added to the bottom of the crucible to deoxidize the steel. Immediately after the Al wire is inserted into the crucible bottom, a molten steel sample was sucked out using a quartz tube and quickly quenched in cold water. After taking the first sample, the oxygen activity of the melt was measured again. The oxygen activities before and after Al addition were 297 ppm and 2.4 ppm, respectively. After that, samples were taken at the crucible bottom with specific time intervals and quenched in cold water. The measured dissolved aluminum at crucible bottom at the initial stage was 0.293%.

After surface being polished, about 1 gram of each steel sample was dissolved in hydrochloric acid solution (1:1 in volume) at 70°C. After the iron matrix was completely dissolved, deionized water was added to dilute the solution. Then, the inclusions were filtered out using a polycarbonate filter paper (0.2-μm pore size) propelled by a vacuum pump. As alumina-based inclusions are insoluble to HCl acid, they will be kept on the filter paper. The extracted inclusions were then observed using SEM after depositing carbon powder over the filter paper under vacuum conditions.

Observation of Single-Alumina Particles

Due to the time-consuming sampling process, the first sample is assumed to be taken 1 min after Al deoxidation; in other words, the holding time is 1 min.

In this sample, a great number of single-alumina particles with different shapes were observed, as shown in Fig. 5. The spherical, dendritic, flower, plate-like, and irregular (such as faceted, polyhedral, cluster, and stick-like) particles were the dominant morphologies. Spherical inclusions were the most (Fig. 5a) and mostly were <2 μm in size, with many of them in sub-micrometer. Singular larger spherical inclusions (up to 3–5 μm in diameter) were also found, and some of them had a faceted feature. Several dendritic inclusions with a large size (>50 μm) were also observed (Fig. 5b). The growth direction of dendritic arms from the nucleus particle was very clear. There are mainly two types of dendritic inclusions: one with only one main growth direction and the other with several growth directions. Furthermore, many flower-shaped clusters were observed (Fig. 5c). These inclusions were similar to the dendritic ones, such as the morphology of arms, clear growth directions, and nucleus particle. But this type of inclusion was with nonsole and more uniform growth directions, nonuniform arm size, as well as shorter and thinner arms and branches. There were also plenty of plate-like inclusions (Fig. 5d). Most of the plate-like inclusions were semitransparent and their sizes were relatively large. Overgrowth on the existing inclusions was observed, which may be the result of a second growth stage from the inclusions when another growth condition was reached. Besides the mentioned inclusion types above, irregular inclusions, including faceted, polyhedral, cluster, and stick-like, were observed in a vast range of sizes (Fig. 5e).

Similar morphologies of inclusions were reported before,[17,27–31] and formation mechanisms of the different-shaped inclusions in steel after deoxidation were also proposed.[28,30,31] Dekkers et al.[28] summarized three factors that had influences on the morphology of inclusions from the point of view of grain growth: supersaturation of the dissolved elements, grain surface roughness, and impurity particles. A mechanism about the transformation of inclusions from polyhedron to dendritic and spherical was pro-
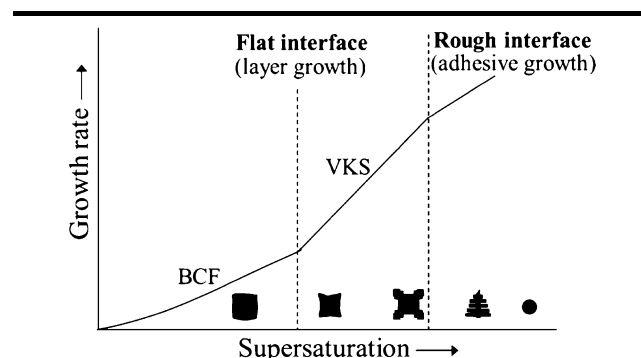

Fig. 6. Different inclusion growth mechanism as a function of generation element supersaturation.[29]
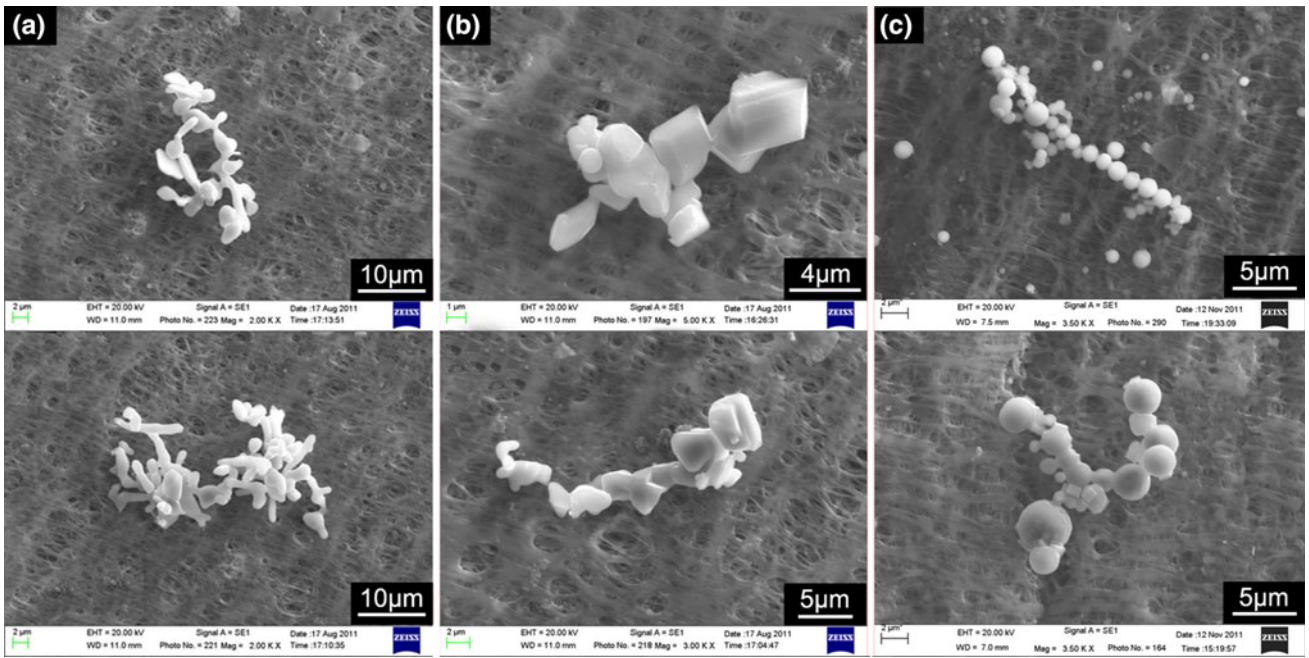
Fig. 7. Different aggregation morphologies before sintering: (a) aggregation of different-shaped single particles; (b) aggregation of polyhedral-shaped particles; and (c) aggregation of spherical-shaped particles.
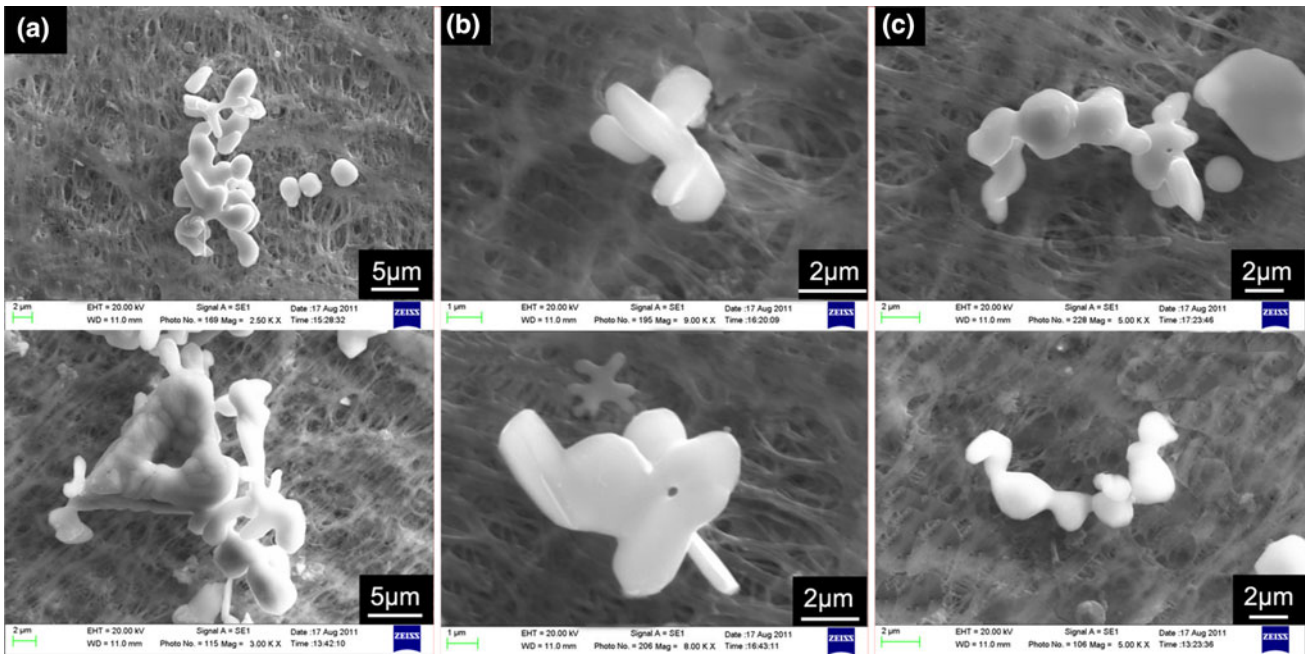

Fig. 8. Different aggregation morphologies after sintering: (a) aggregation of different-shaped particles; (b) aggregation of polyhedral-shaped particles; and (c) aggregation of spherical-shaped particles.

posed, as shown as Fig. 6.[29,32] In the figure, VKS means the Volmer–Kossel–Stranski model for two-dimensional nucleation, and BCF is the Burton–Cabrera–Frank model for spiral growth.[32]

The morphology of single-alumina particles after deoxidation greatly depends on the supersaturation of deoxidizing elements, calculated by Eq. 13.

$$S = \frac{a_{[O]}^3 \cdot a_{[Al]}^2}{\left(a_{[O]}^3 \cdot a_{[Al]}^2\right)_{eq}} = \frac{a_{[O]}^3 \cdot a_{[Al]}^2}{K_{Al_2O_3}} \quad (13)$$

where S is the supersaturation degree; $a_{[O]}$ and $a_{[Al]}$ are the activities of dissolved oxygen and aluminum,
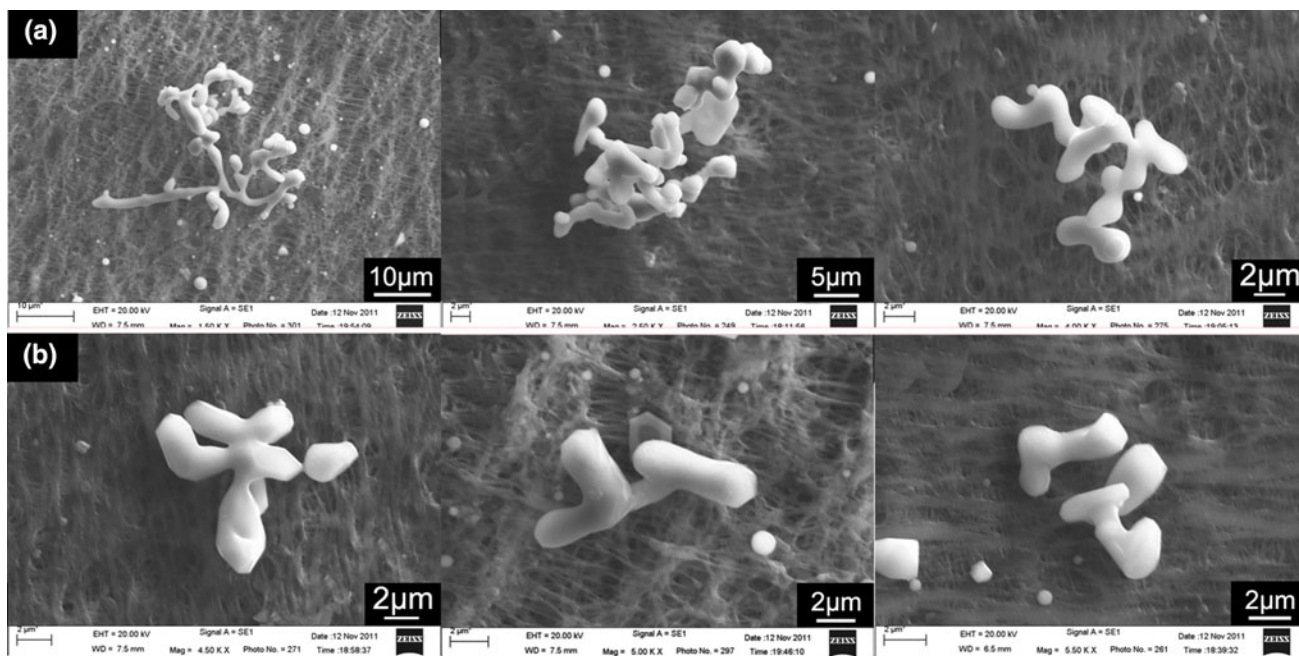
Fig. 9. Morphology of coral-shaped inclusions: (a) aggregation of different-shaped particles and (b) aggregation of polyhedral- or spherical-shaped particles.

respectively; and $K_{Al_2O_3}$ is the equilibrium constant of Al_2O_3 generation.

In the current work, after Al addition, the dissolved oxygen and aluminum were 0.0297% and 0.293%, respectively, leading to a very high supersaturation degree. Thus, with the decrease of supersaturation caused by the deoxidation reaction and the diffusion of the dissolved aluminum, the generation order of alumina particles is spherical first, and then dendrite, flower, plate-like, and polyhedron subsequently. When the saturation gradient is in one main direction or there is only one suitable precipitation location on the nucleus, a one-arm dendritic inclusion precipitate exists, while a dendritic inclusion with a several-arms precipitate when there are several saturation gradient directions around the nucleus and several suitable precipitation location exist simultaneously. When the saturation gradient direction always changes during the growth of the inclusion, clusters with an irregular-shaped precipitate. Due to the decrease and the uniformity of supersaturation, flower-shaped inclusions existed with shorter arms and a uniform growth direction precipitate. The plate-like inclusions with angles or arms may be generated during the transitional stage between the adhesive growth and the layer growth.

Observation of Alumina Aggregation

As the holding time after deoxidation increased, some of the alumina particles would be aggregated owing to the collision with each other. As time increased further, the morphology of the aggregated clusters might be changed as well.

Figure 7 presents the different aggregation morphologies before sintering, including aggregation of several different-shaped particles, aggregation of polyhedral-shaped particles, and aggregation of spherical-shaped particles. It is worthy to note that the aggregation of irregular-shaped inclusions was disordered while the polyhedral-shaped and spherical-shaped inclusions was aggregated one by one. Before sintering, the single particles in the aggregated inclusions touched each other by a limited area, and retained their original morphologies.

After sintering, as shown in Fig. 8, the component particles were sintered together with a larger connecting area and more curved boundary line. Some shrinkage holes were found in the inclusion on the lower left of the figure.

The typical morphologies of extracted inclusions in the sample with holding time of 17 min are presented in Fig. 9, indicating that the aggregating boundary line almost disappears, and the surface of the inclusions becomes denser and more smooth, which let inclusions transform into a coral shape. The studies by Zhang et al.[14] reported that this morphology is induced by the process of Ostwald ripening by which small inclusions and the sharp edge of inclusions are dissolved and larger inclusions grow.

CONCLUSIONS

The calculation of the thermodynamics for homogeneous nucleation of alumina and the three-

dimensional observation of alumina morphologies after Al-O reaction were carried out. It is indicated by the calculation that, when the interfacial tension between steel melt and alumina is higher or the nucleus radius is larger, it is harder for alumina to nucleation. On the other hand, the possible nucleus radius could be estimated according to the concentration of aluminum and oxygen. One minute after the deoxidation reaction in laboratory, a great number of single-alumina particles with different shapes, including spherical, dendritic, flower, plate-like, and irregular, were observed. The formation of various shapes is due to different growth mechanisms. During the holding process after deoxidation, several types of aggregation morphologies were observed, such as disorderly type and regular type. Owing to the effects of sintering and Ostwald ripening, the aggregated inclusions changed from angular shape to smooth coral shape.

ACKNOWLEDGEMENTS

REFERENCES

1. C. Bonilla, *Ironmak. Steelmak.* 22, 41 (1995).
2. H. Yasunaka, R. Yamanaka, T. Inoue, and T. Saito, *Tetsu-To-Hagane* 81, 529 (1995).
3. G. Domizzi, G. Anteri, and J. Ovejero-Garcia, *Corrosion Sci.* 43, 325 (2001).
4. S. Basu, S.K. Choudhary, and N.U. Girase, *ISIJ Int.* 44, 1653 (2004).
5. Ø. Grong, L. Kolbeinsen, C. van der Eijk, and G. Tranell, *ISIJ Int.* 46, 824 (2006).
6. D.S. Sarma, A.V. Karasev, and P.G. Jonsson, *ISIJ Int.* 49, 1063 (2009).
7. J.S. Byun, J.-H. Shim, Y.W. Cho, and D.N. Lee, *Acta Mater.* 51, 1593 (2003).
8. F. Ishikawa, T. Takahashi, and T. Ochi, *Metall. Mater. Trans. A* 25, 929 (1994).
9. H. Itoh, M. Hino, and S. Ban-ya, *Tetsu-to-Hagane* 83, 623 (1997).
10. H. Itoh, M. Hino, and S. Ban-ya, *Tetsu-to-Hagane* 83, 773 (1997).
11. H. Itoh, M. Hino, and S. Ban-ya, *Tetsu-to-Hagane* 83, 695 (1997).
12. H. Lei, K. Nakajima, and J.-C. He, *ISIJ Int.* 50, 1735 (2010).
13. J. Zhang and H.-G. Lee, *ISIJ Int.* 44, 1629 (2004).
14. L. Zhang and W. Pluschkell, *Ironmak. Steelmak.* 30, 106 (2003).
15. L. Zhang, S. Taniguchi, and K. Cai, *Metall. Mater. Trans. B* 31, 253 (2000).
16. Y. Kwon, J. Zhang, and H.-G. Lee, *ISIJ Int.* 46, 257 (2006).
17. Y. Jin, Z. Liu, and R. Takata, *ISIJ Int.* 50, 371 (2010).
18. H. Ohta and H. Suito, *ISIJ Int.* 46, 14 (2006).
19. M.L. Turpin and J.F. Elliott, *J. Iron Steel Inst.* 204, 217 (1966).
20. D. Hilty and W. Crafts, *Trans. AIME* 188, 414 (1950).
21. I. Novokhatsky and B. Belov, *Izvest. Akad. Nauk SSSR* (3), 15 (1969).
22. L. Rohde, A. Choudhury, and M. Wahlster, *Arch. Eisenhuttenwesen* 42, 165 (1971).
23. H. Schenck, E. Steinmetz, and K. Mehta, *Arch. Eisenhuttenwesen* 41, 131 (1970).
24. H. Suito, H. Inoue, and R. Inoue, *ISIJ Int.* 31, 1381 (1991).
25. K. Wasai and K. Mukai, *Metall. Mater. Trans. B* 30, 1065 (1999).
26. K. Wasai and K. Mukai, *ISIJ Int.* 42, 467 (2002).
27. R. Dekkers, B. Blanpain, and P. Wollants, *ISSTech 2003 Conference Proceedings*, 2003, pp. 197–209.
28. R. Dekkers, B. Blanpain, and P. Wollants, *Metall. Mater. Trans. B* 34, 161 (2003).
29. R. Dekkers, B. Blanpain, P. Wollants, F. Haers, C. Vercruyssen, and B. Gommers, *Ironmak. Steelmak.* 29, 437 (2003).
30. M.A. Van Ende, M.X. Guo, E. Zinngrebe, R. Dekkers, J. Proost, B. Blanpain, and P. Wollants, *Ironmak. Steelmak.* 36, 201 (2009).
31. K. Wasai, K. Mukai, and A. Miyanaga, *ISIJ Int.* 42, 459 (2002).
32. I. Sunagawa, *Morphology of Crystals, Part B1987* (Tokyo, Japan: Terra Scientific Publishing, 1987).